Dissipative Solitons and Switching Waves in Dispersion-Modulated Kerr Cavities

Miles H. Anderson, Alexey Tikan, Aleksandr Tusnin, Johann Riemensberger, Alisa Davydova, Rui Ning Wang, and Tobias J. Kippenberg*

Institute of Physics, Swiss Federal Institute of Technology (EPFL), Lausanne, Switzerland and Center for Quantum Science and Engineering, EPFL, Lausanne, Switzerland

(Received 19 June 2022; accepted 14 February 2023; published 16 March 2023)

We theoretically and experimentally investigate the formation of dissipative coherent structures in Kerr nonlinear optical microresonators, whose spectrum encompasses an integrated dispersion that exceeds the cavity free-spectral range. We are able to access this regime in low-dispersion photonic chip-based microresonators by employing synchronous pulse driving, which increases the peak power over the continuous-wave-driving regime. Exploring this dispersion-folded regime, we demonstrate that the presence of periodically varying dispersion can excite higher-order comb structures, which we explore in both the normal and anomalous dispersion regimes. In the former, we observe the coexistence of switching wave fronts with Faraday instability-induced period-doubling patterns. They manifest as strong satellite microcombs highly separated either side of the core microcomb, at an offset close to half the repetition rate but while sharing the same repetition rate. In the latter, for dissipative Kerr solitons in anomalous dispersion, we observe the formation of higher-order phase-matched dispersive waves ("Kelly-like" sidebands), where the folded dispersion crosses the frequency comb grid. We observe up to the fifth higher-order dispersive wave in our experiments and show that these higher-order dispersive waves coherently extend the soliton frequency comb bandwidth significantly. For both cases, we show that our results can be understood by considering four-wave mixing in a two-dimensional Fourier transform representation. The results demonstrate the rich novel nonlinear dynamics of driven dissipative nonlinear cavities with periodically varying dispersion in the dispersion-folded pumping regime.

DOI: 10.1103/PhysRevX.13.011040 Subject Areas: Optics, Photonics

I. INTRODUCTION

Nonlinear pattern formation is a fascinating phenomena and ubiquitous in nature [1]. Over the past decade, a wide variety of dissipative coherent structures in continuous-wave-driven Kerr optical nonlinear microresonators has been observed and studied [2,3]. It is now well understood that two fundamental localized dissipative structures can be generated via parametric interactions in microresonators: dissipative Kerr solitons (DKSs) in anomalous dispersion [4] and switching waves (SWs) [5,6] (otherwise termed as platicons or "dark pulses" in certain configurations) in the normal dispersion regime, which in the cw-driven case are excited by mode-crossing-induced dispersion changes [7]. Both structures are governed by the Lugiato-Lefever equation (LLE) and constitute coherent optical frequency combs in the frequency domain. Such "microcombs," DKS-based microcombs, in particular, have expanded the domain of optical frequency combs and have been used in numerous system level applications, due to their high repetition rates in the microwave domain and their compact chip-integrated form factor, into various application domains—including neuromorphic computing [8], ultrafast ranging and parallel coherent LIDAR [9,10], coherent telecommunications [11], astronomical spectrometer calibration [12], frequency synthesizers [13], and atomic clock architectures [14]. Given that a comprehensive understanding of the nonlinear dynamical physics of dissipative Kerr structures in conventional optical microresonators and fiber cavities has emerged, recently significant attention has been devoted to exploring physics and microcomb generation in nontrivial regimes. These regimes include alternative pumping schemes such as pulse driving [15] or self-injection locked lasers [16,17], as well as the study of complex dispersion profiles to extend the comb bandwidth of solitons with dispersive waves (DWs) [13,18]. Indeed, recent work highlights the novel dynamics associated with complex resonator structures such as microresonators with integrated Bragg gratings and photonic-crystal elements [19], as well as the emergent nonlinear dynamics observed in coupled microring photonic "dimers" [20], i.e., photonic "molecules" [21].

*tobias.kippenberg@epfl.ch

Yet, in nearly all prior experimental studies of driven nonlinear optical microresonators, the Kerr frequency shift has been, heuristically, less than the free-spectral range (FSR). In other words, the spectral extent of the generated coherent dissipative structure exhibits an integrated dispersion that is smaller than the free-spectral range. This is predominantly the natural regime for typical microresonators with a large FSR over approximately 50 GHz. Here, we study the nonlinear dynamics beyond this realm. Using pulsed optical pumping [15,22] of low-repetition-rate optical microresonators, we access the regime where the "dissipative structures" cover a bandwidth whose integrated dispersion exceeds the FSR of the resonator. Akin to electrons in periodic bands that give rise to the Brillouin zone, we demonstrate how dispersion folding can occur. Specifically, when the dispersion folds back to the zone spanned by the FSR, we show that any periodic perturbation of the soliton during its round-trip (in our case produced by introducing spatially varying dispersion) enables quasiphase matching for emergent higher-order structures at the edge of the dispersion "zone." In this way, periodic forcing of the cavity field every round-trip via the dispersion constitutes a form of parametric driving. For solitons, this gives rise to higher-order dispersive waves [23,24], also identified as "Kelly sidebands" historically discovered in systems with periodic amplification and later soliton fiber lasers [25–28]. Additionally, in cw-driven systems, dispersion modulation, or, in fact, parametric modulation of any system parameter, has long been known to lead to Faraday instability (FI). FI patterns were most originally studied in vertically shaken fluid basins [29] and were observed to occur oscillating first at half the forcing frequency. From a general point of view, such dynamics in optical resonators are governed by partial differential equations with periodic coefficients. The associated field of study is called Floquet theory. Floquet dynamics and consequent optical FI has been discussed earlier mostly in the context of fiber-based devices [30–33] operating in the quasi-cw regime where period-doubling dynamics [34] as well as the competition between Turing and Faraday instability [35,36] have been observed. The very same dynamics have also been studied for Bose-Einstein condensates [37].

In this work, we provide experimental observation of higher-order (fifth) dispersive waves bound to a dissipative Kerr soliton microcomb, and the generation of strong satellite combs in a switching wave microcomb, powered by FI pattern formation not yet seen or studied in photonic microresonators. In the latter, this results in a 5× extension of the total comb bandwidth. Reconstructing the absolute optical frequencies, we show that the satellite combs share the same comb line spacing but a different offset frequency. For both cases of normal and anomalous dispersion, we theoretically analyze the dynamics behind the periodically perturbed LLE using the paradigm of two-dimensional (2D) four-wave mixing (FWM) in the unfolded dispersion space. As such, we derive and analyze theoretically the two-dimensional version of the LLE that describes this physical reasoning. Finally, we apply the notion of the nonlinear dispersion relation (NDR) to this system, which reveals the complex photon transfer pathways underlying the process of sideband formation. Our results endeavor to expand the conventional understanding about dispersion by studying the consequence of dispersion folding.

II. GENERAL MODEL OF DISPERSION-MODULATED CAVITY

The fundamental model underpinning all the phenomena presented and discussed in this work is depicted in Fig. 1. The resonator can be represented as a waveguide ring [Fig. 1(a)] whose cross section varies in such a way that the group velocity dispersion parameter $d_2(z)$ (β_2 or D_2 as it is in the experimental sample) varies periodically over length L and amplitude Δ or in the time domain as $t = z/D_1R$ for resonator with radius R and FSR D_1. The system can be evaluated piecewise as in Fig. 1(b), where the underlying integrated dispersion operator $d_{\mathrm{int}} = d_2\mu^2$ varies for each step in direction z [Fig. 1(c)]. The concept of FSR dispersion folding [see Fig. 1(d)] serves as a convenient visual representation of the process of phase-matched FWM in the cavity. The dispersion curve passing FSR/2 is folded back to −FSR/2. In this picture, momentum mismatch between the branches of dispersion is not compensated in nonmodulated cavities. Thus, FWM interactions with folded modes become resonant only when there is a mechanism coupling two neighboring FSRs.

To establish a clear line of reasoning and understand the dynamics of this system, we revisit and extend conclusions presented in previous studies [32–35], looking at them from a different point of view that employs the notion of two-dimensional four-wave mixing (2D FWM).

A. Model

To model the nonlinear dynamics of the cavity with periodically modulated dispersion, we use a well-known form of the LLE with a time-dependent dispersion term [32]. In dimensionless units, the equation takes the form

$$\frac{\partial\Psi}{\partial t} = -(1 + i\zeta_0)\Psi + i[d_2^{(0)} + d_2(t)]\frac{\partial^2\Psi}{\partial\varphi^2} + i|\Psi|^2\Psi + f(\varphi), \tag{1}$$

where $\Psi(\varphi, t)$ describes the slowly varying envelope of the optical field in the microresonator, $f(\varphi)$ is the driving function (which may be a pulse profile), φ is the azimuthal coordinate inside the cavity in the frame moving with velocity $d_1 = 2D_1/\kappa$ with $D_1 = 2\pi \cdot \mathrm{FSR}$, $\zeta_0 = 2\delta\omega_0/\kappa$ is the normalized laser-cavity detuning, and $\kappa = \kappa_0 + \kappa_{\mathrm{ex}}$ is the total linewidth of the resonator with internal linewidth

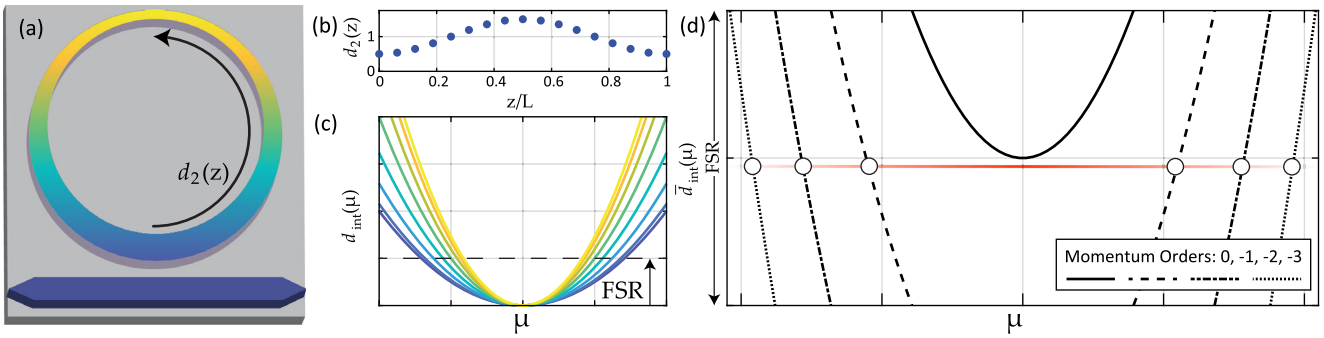

FIG. 1. Model for dispersion zone folding in driven dissipative Kerr nonlinear microresonators. (a) The simplest case of a passive nonlinear microresonator whose waveguide width, and thus dispersion parameter, undergoes a periodic cycle. (b) In our modeling, we consider a simple sinusoidal dispersion modulation, evaluated piecewise. (c) The integrated dispersion of each resonator mode μ along the microresonator's circumference, for each value of d_2 plotted in (b). (d) Round-trip integrated dispersion, this time plotted in the folded zone over one free-spectral range. The comb spectrum spans multiple orders of dispersion, but each higher order is phase mismatched. Dispersion modulation is required to quasiphase match.

κ_0 and coupling to the bus waveguide κ_{ex}. Dispersion coefficients $d_2^{(0)}$ and $d_2(t)$ and time t are normalized on the photon lifetime so that $d_2 = D_2/\kappa$ and $t = t'\kappa/2$ for real lab time t'. In this model, we denote $d_2^{(0)}$ as the averaged resonator dispersion with periodic modulation $d_2(t+T) = d_2(t)$, where $T = T'\kappa/2 = \pi\kappa/D_1$ is the normalized round-trip time. If the driving function $f(\varphi, t)$ is also periodic in time with period T, we can assume that the field Ψ has the same symmetry $\Psi(t+T) = \Psi(t)$, and we can employ the Fourier transform

$$d_2(t) = \sum_n \tilde{d}_2^{(n)} e^{-id_1 nt}, \tag{2}$$

$$\Psi(\varphi, t) = \sum_{n\mu} \tilde{\psi}_{n\mu} e^{i\mu\varphi - id_1 nt} \tag{3}$$

and obtain an effective two-dimensional equation governing the Floquet dynamics (here, f is taken constant for simplicity, but the equation can be readily generalized):

$$\begin{aligned}\frac{\partial\tilde{\psi}_{n\mu}}{\partial t} = &-(1 + i[\zeta_0 - nd_1] + id_2^{(0)}\mu^2)\tilde{\psi}_{n\mu} \\ &- i\sum_m \tilde{d}_2^{(n-m)}\mu^2\tilde{\psi}_{m\mu} + i\sum_{\substack{n_1,n_2,n_3 \\ \mu_1,\mu_2,\mu_3}} \tilde{\psi}_{n_1\mu_1}\tilde{\psi}_{n_2\mu_2}\tilde{\psi}^*_{n_3\mu_3}\delta_{\mathrm{FWM}} \\ &+ \delta_{n,0} f,\end{aligned} \tag{4}$$

where the conservation law $\delta_{\mathrm{FWM}} = \delta(\mu_1 + \mu_2 - \mu_3 - \mu)\delta(n_1 + n_2 - n_3 - n)$ governs 2D FWM processes in the fast- (μ) or slow- (n) frequency space. We can, thus, conclude that the periodically varying dispersion, which in the LLE leads to a time-dependent dispersion term, couples different Floquet orders (n) of the intracavity field.

The dispersionless profile along n (modes are equidistant in this direction having D_1 frequency spacing) protects our system from transverse instabilities [38,39], allowing us to study and generalize well-known coherent structures such as DKSs and SWs. However, the presence of periodic dispersion modulation results in linear coupling between different orders of Floquet index n that effectively correspond to FSR-frequency breathing. As shown in Eq. (4), the coupling amplitude is proportional to the Fourier coefficients $\tilde{d}_2^{(n)}$ and scales *quadratically* with comb index μ, increasingly strengthening the coupling rate for larger mode numbers $|\mu|$.

B. Upper- and lower-state perturbation

To demonstrate the effect of dispersion modulation on the cavity dynamics for all comb modes, we provide split-step simulations [40] of Eq. (1), shown in Fig. 2. We first investigate the effect of phase matching on the noise transduction properties of the cavity, in the *absence* of any coherent structure formation to avoid the effect of conventional modulation (Turing) instability [32]; we simulate the case of a low average normal dispersion ($d_2^{(0)} = 0.0027$). Given a cw driving strength of $f^2 = 10$, typical for the generation of solitons or switching waves, the Kerr nonlinear cavity possesses a bistable condition across a range of detuning to approximately $\zeta_0 < 10$, with an upper and lower cw-state solution Ψ_H and Ψ_L, respectively (solutions of which are in Appendix A). In Figs. 2(a) and 2(c), corresponding to the respective lower and upper states, we show the long-term response to small noise continuously placed on each comb mode, revealed by taking the 2D Fourier transform of the output fast-time domain field recorded over a large number of round-trips, with a numerical integration step smaller than the cavity

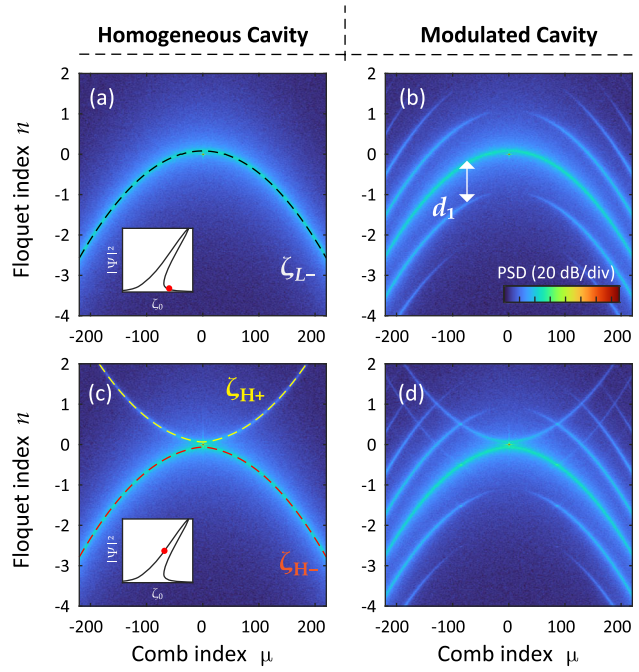

FIG. 2. Dispersion curves or Floquet bands for homogeneous and modulated cavity. (a),(c) Simulated 2D Fourier transform for light propagating in the Kerr lower state at $\zeta_0 = 5$ and upper state at $\zeta_0 = 4$, respectively, in a homogeneous cavity with normalized driving strength $f^2 = 10$. The conjugated dispersion curve is apparent only in the upper state. (b),(d) The same solution existing in a dispersion-modulated cavity with $\Delta = 0.5d_2^{(0)}$, $d_1/2\pi = 8$, and $d_2^{(0)} = 0.0027$.

round-trip. Such a figure is henceforth referred to as the NDR, used in optics and hydrodynamics to describe complex nonlinear systems [20,41,42]. It can be expressed as follows:

$$\mathrm{NDR}(\Omega,\mu) = \frac{1}{\sqrt{N_t N}} \sum_{\ell,k} \Psi_{\ell,k} e^{i(\Omega t_k - 2\pi\mu\ell/N)}, \tag{5}$$

where Ω is a slow frequency, $t_k = \Delta t k$ with $\Delta t = T_l/N_t$ time step, and T_l is simulation time with N_t the number of discretization points. Figure 2 presents the power spectral density of the NDR over Floquet index n vs μ, which are, respectively, proportional to the "slow: frequency Ω counted in D_1 and longitudinal mode (comb) index.

Each state carries conjugate pairs of resonant radiation conditions related to the dispersion operator [43,44], originating from the two states Ψ_H and Ψ_L: $\zeta_{H\pm}$ and $\zeta_{L\pm}$, respectively (see Appendix A). Our simulations reveal that the noise within the cavity forms a prominent resonance curve that follows one of those dispersion relations, depending on which bistable state the field is in. We note that the conjugated ζ_+ relation appears weakly only on the upper state [depicted as ζ_{H+} in Fig. 2(c)] as a result of sufficient FWM with ζ_{H-}. In Figs. 2(b) and 2(d), we see how rapid dispersion frequency modulation causes this radiation condition to carry sidebands, hence referred to as Floquet bands, spaced along the n axis spaced by d_1 ($n = \zeta/d_1$). For this simulated example, $d_1/2\pi = 8$, corresponding to 8 times the photon lifetime frequency. For simplicity, we consider an example of $\tilde{d}_2^{(1)} = \tilde{d}_2^{(-1)} = \Delta/2$ that corresponds to cosine modulation of the dispersion. In this case, the linear term in Eq. (4) couples n and $n \pm 1$ frequency modes with a coupling strength $\Delta\mu^2/2$. This effect is similar to sideband generation in electro-optic modulation, in which efficiency increases with the mode number μ. Strikingly, *both* upper-state Floquet bands ζ_{H-} and ζ_{H+} are affected by the modulation in a similar way, as shown in Fig. 2(d).

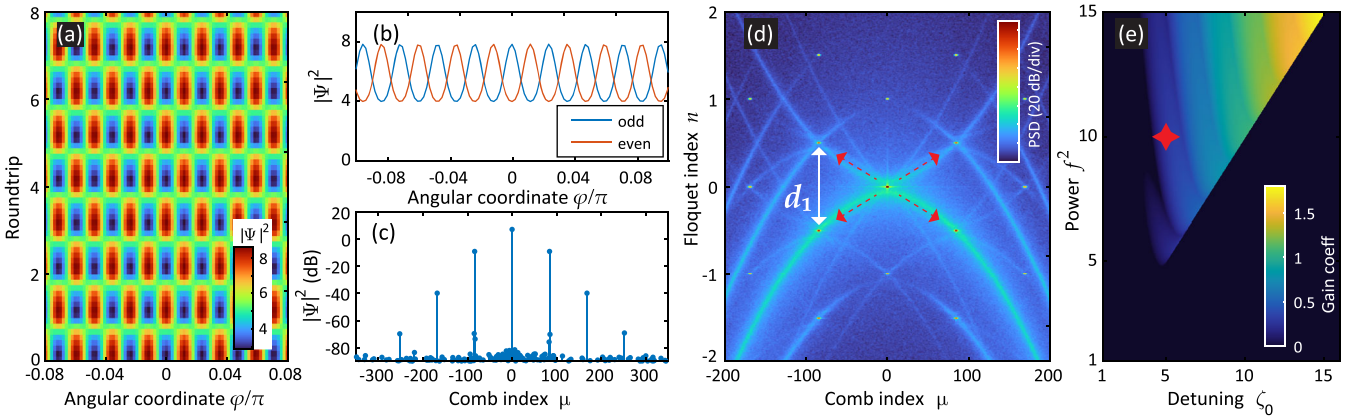

FIG. 3. FI simulation in a cw-driven Kerr cavity with normal dispersion for a cavity with $f^2 = 10$, $\zeta_0 = 5$, $\Delta = 0.5d_2^{(0)}$, $d_1/2\pi = 8$, and $d_2^{(0)} = 0.0027$. (a) Fluctuating field over round-trips vs angular coordinate. (b) Angular coordinate domain showing two consecutive cavity round-trips. (c) Fast frequency domain snapshot. (d) 2D Fourier transform (NDR) of (a) for Floquet mode index n vs comb mode index μ. (e) Gain coefficient for FI as a function of the detuning and power. Red star marks the operating point for (a)–(d).

C. Faraday instability

To reveal the emergence of FI, we modify the simulations presented in Fig. 2(d) entering the range of parameters corresponding to the unstable regime. The above-mentioned simplification allows us to further develop an analytical derivation and analyze the linear stability of the system. We use a conventional stability analysis approach [45] but in the new 2D FWM setting created by Eq. (4), assuming FSR/2 periodic dynamics of the field. As a result, we obtain that comb indices corresponding to the maximum FI gain can be approximated by the following expression (see Appendix A 2):

$$\mu \approx \pm \sqrt{\frac{d_1}{2\sqrt{(d_2^{(0)})^2 - \Delta^2}}} \approx \pm \sqrt{\frac{D_1}{D_2^{(0)}}}. \tag{6}$$

Equation (6) reveals that, in the normal dispersion regime, it is possible to observe formation of sidebands *with a frequency offset* of FSR/2 from the pump which is also highlighted in Fig. 3. Figures 3(a)–3(e) show the result of the numerical simulations. The considered range of parameters corresponds to period-doubling dynamics in the resonator with a $2T$ oscillation period, similar to results in Ref. [34]. Figures 3(a) and 3(b) show a corresponding spatiotemporal diagram and its cross sections at two states separated by T. The NDR shown in Fig. 3(d) shows the 2D nature of the FWM pathways, implying that pump photons can be transferred in the 2D frequency space by changing both μ and n indexes. The maximum FI gain [see Fig. 3(e) for the full FI gain diagram] is placed at the modes corresponding to a $d_1/2$ spacing between the ζ_{H+} and ζ_{H-} Floquet bands.

III. ANOMALOUS DISPERSION CASE

A. Numerical analysis

First, we revisit the effect of the perturbation on the bright DKS formed in the anomalous dispersion cavity. The exact distribution of the modulation along the cavity can affect the position or the amplitude of the instability gain. However, this does not change overall dynamical features [32], which allows us to use the simplest cosine-modulated cavity. Although the Faraday instability gain can be positive, in this case [35], the cw solution on the upper branch is Turing unstable [46] and, in the considered range of parameters, leads to DKS generation. Therefore, dispersion modulation here acts as a round-trip-periodic perturbation to a stable DKS state. This provides a photon-transferring mechanism—quasiphase matching—resulting in power enhancement in certain modes placed at the same frequency grid as the soliton line. They modify the solitonic spectrum with Fano-shaped sidebands (also known as Kelly sidebands) [24], which we refer to as here as higher-order dispersive waves (HDWs). "Higher-order" in this sense is explicitly related to the Floquet dimension (modulation in the longitudinal axis) and should not be confused with higher *polynomial* orders of the dispersion d_4, d_5, etc.

To illustrate this, we repeat numerical solutions to Eq. (1). In Figs. 4(a), 4(b), and 4(d), we recall the conventional (unperturbed) DKS features. Figure 4(a)

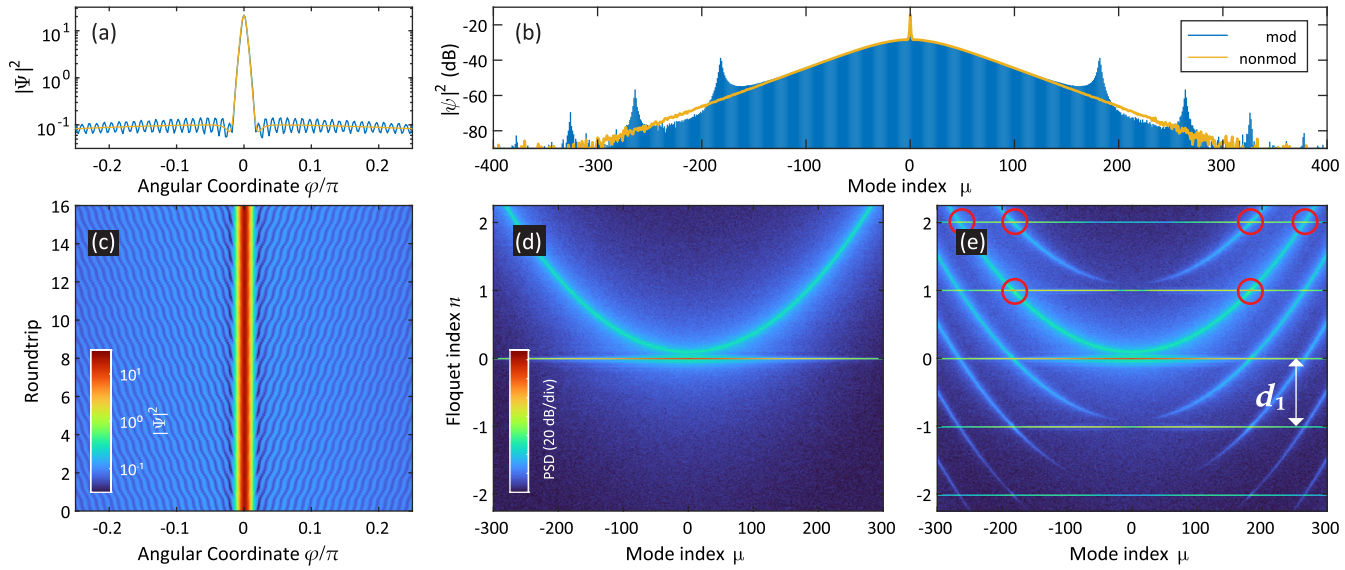

FIG. 4. DKS simulation in cw-driven modulated cavity for $f^2 = 10$, $\zeta_0 = 10$, $\Delta = 0.7d_2^{(0)}$, $d_1/2\pi = 16$, and $d_2^{(0)} = -0.0027$. (a) DKS field in cavity angular coordinate with (blue) and without (yellow) modulation. (b) Corresponding fast frequency power spectrum. (c) Spatiotemporal diagram of the modulated DKS propagating over resonator round-trips (slow time). (d),(e) DKS nonlinear dispersion relations, obtained by taken $\mathcal{F}[\,]$ over both dimensions of the spatiotemporal diagram for nonmodulated and modulated cases, respectively. Red circles show higher-order dispersive wave positions.

(yellow) shows a cross section which contains a secant hyperbolic profile on a cw background. The frequency domain of this is shown in Fig. 4(b). Taking the 2D Fourier transform of the spatiotemporal data, we obtain NDR (described above), in Fig. 4(d). The NDR of a single unperturbed soliton has two components: a soliton line and the dispersive resonance curve ζ_{L-}, which is seeded mainly by the cavity noise and here is approximately equal to the cold-cavity dispersion operator. The detuning of the DKS from the cold-cavity resonance ζ_0 is given by the gap between the soliton line and the ζ_{L-} curve. Crucially, even though the cavity dispersion wraps over the FSR line $n = 1$ more than once, *no dispersive wave* is created in this case, since the nonlinear photon transfer is forbidden by the momentum conservation law [47].

When periodic dispersion modulation is introduced, we observe a different picture [Figs. 4(a)–4(c) and 4(e)]. The spatiotemporal diagram (c) reveals that DKS starts to radiate dispersive waves to the cavity, depicted by wavy lines emanating from the DKS and overlapping every round-trip. They appear as a cw background modulation shown in Fig. 4(a) and in Fig. 4(b) are seen to be several HDW on the spectral wings (i.e., Kelly sidebands). The NDR presented in Fig. 4(e) reveals that the HDW originate from the intersection between the soliton line and the FSR-folded Floquet bands. This interaction is enabled by the periodic modulation which couples neighboring modes, appearing in the NDR as copies of the soliton line and dispersive Floquet bands repeated at every FSR. In this way, the momentum conservation law can be satisfied which leads to efficient nonlinear photon transfer at the intersection points, forming the HDW in the spectrum. An extended 3D perspective and a view of the dispersion-folded space can be found in Supplemental Material [48].

B. Experimental setup

The experimental setup used for all the experimental results of this work is presented in Fig. 5. The resonators of choice [one pictured in Fig. 5(a)] are based on the photonic Si_3N_4 waveguide platform, fabricated using the *Damascene process* [49], and have an FSR of 15 GHz. While the ring resonator in the theoretical model is assumed to have a sinusoidally varying second-order dispersion D_2, the real resonators are more complex. The original motivation for inserting a single mode section into the resonators was to suppress mixing between higher-order transverse modes, that can lead to single-mode dispersive waves. However, as detailed below, we find that this leads to new dynamics. This is achieved with the use of a higher-order mode suppression section (MSS), a short segment of the resonator where the waveguide tapers from its main waveguide width down to 0.4 μm [50,51], a

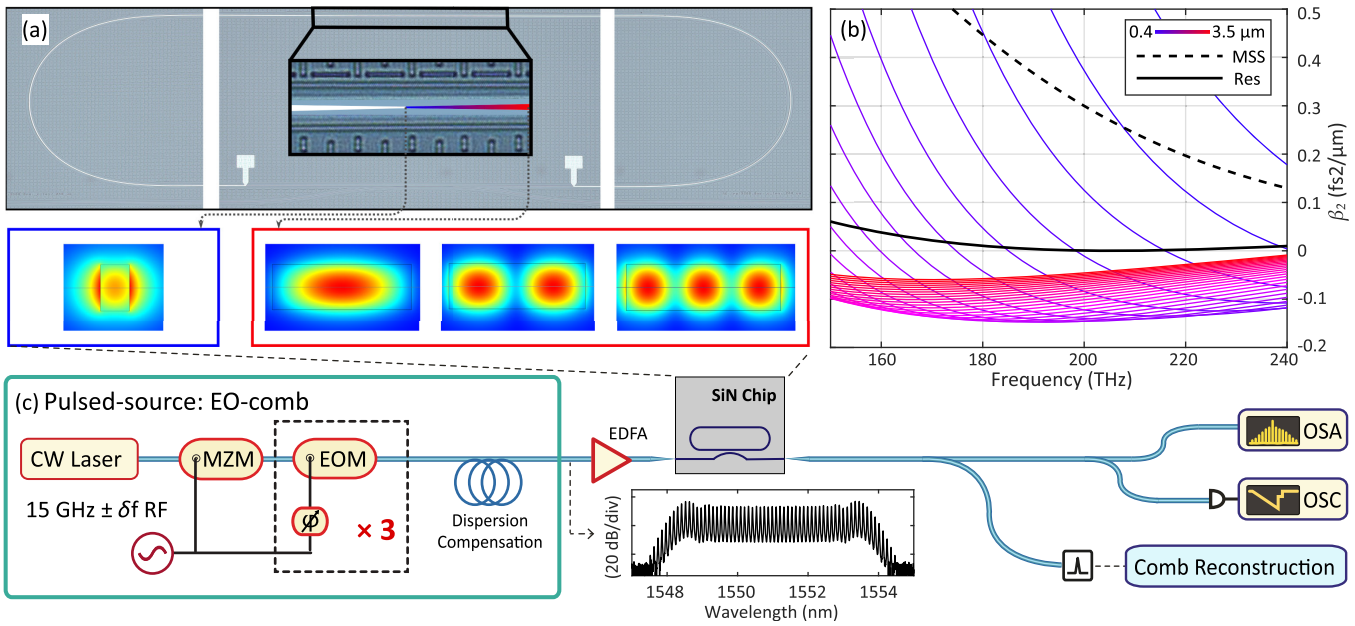

FIG. 5. Si_3N_4 photonic chip and experimental setup. (a) Microscope image of the Si_3N_4 racetrack microresonator having 15 GHz free-spectral range. The inset shows the mode suppression section (MSS). The variation of the waveguide width is highlighted by the color gradient. (b) The variation of the dispersion over the MSS for changing waveguide width (height = 820 nm), the aggregate dispersion of the whole MSS, and the aggregate dispersion for the whole resonator. (c) Experimental chip pumping scheme, featuring the EO comb as a pulsed source. The input pulse train is coupled into and out of the microresonator chip via lensed fibers. Bottom inset: spectrum of the 15 GHz EO comb before amplification. MZM, Mach-Zehnder modulator; EOM, electro-optic modulator; EDFA, erbium-doped fiber amplifier; OSA, optical spectrum analyzer; OSC, oscilloscope. See Supplemental Material [48] for description of "comb reconstruction" section.

width where only the fundamental mode may propagate without strong loss, shown in Fig. 5(a). In Fig. 5(b), we plot numerically calculated waveguide dispersion values β_2 for several discrete waveguide cross sections along the MSS, showing how the dispersion transitions from weakly anomalous up to strongly normal. We can retrieve the *average* round-trip dispersion $\beta_2^{(0)}$ through a weighted sum of β_2 for each waveguide width according to their relative length. In this example resonator design, the final aggregate dispersion calculation comes out close to zero, since the MSS accounts for 13% of the total cavity length. This also means the dispersion modulation duty cycle is not pure sinusoidal but rather more pulselike with many more coupling harmonics in the longitudinal n-space. For numerical modeling presented below, we assume a pure sinusoidal approximation, but a full pulselike treatment for the dispersion can be found in Supplemental Material [48]. The final average resonator dispersion value is found through

$$D_2^{(0)} = -\beta_2^{(0)} L D_1^3 / 2\pi. \tag{7}$$

Resonators fabricated with this architecture for the experiment include a range of average dispersion values from anomalous to normal, providing the results for both regimes in this work.

The pumping and measurement setup itself is presented in Fig. 5(c). In order to reach the required driving powers for the regime where the Floquet dynamics due to the presence of dispersion bands can be accessed and to ensure the generation of a single dissipative structure, pulse driving using an electro-optic (EO) comb is employed [52] as has been done previously for experiments in resonators with a similar gigahertz-domain FSR [15,22,53]. A full breakdown of the components used is given in Ref. [22]. It yields a pulse train of pulses approximately 1.4 ps in duration with an rf controllable repetition rate f_{eo} set near 15 GHz (see Appendix C for further details).

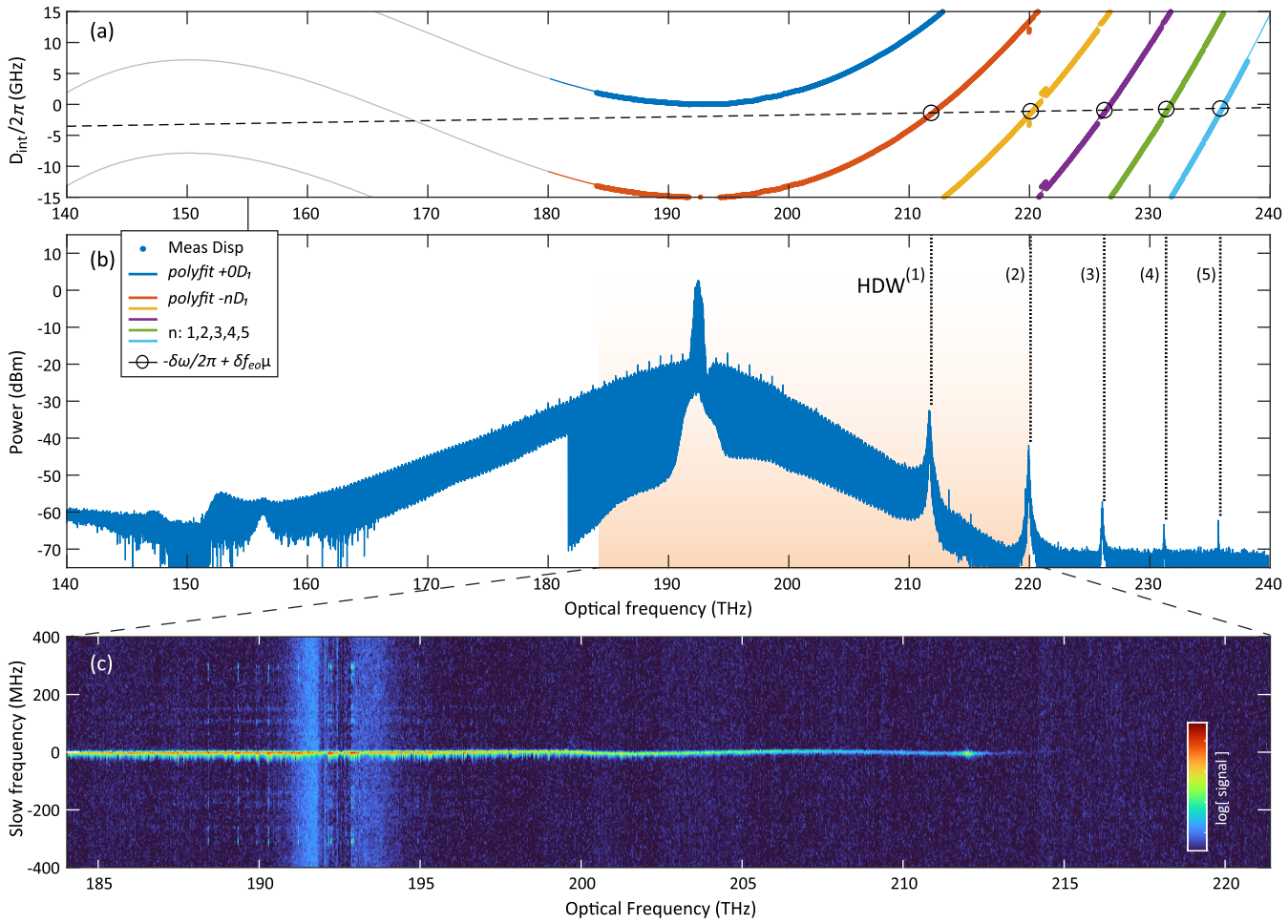

FIG. 6. Dissipative soliton with higher-order dispersive wave experiment. (a) Measured integrated dispersion profile overlaid against polynomial fit, including all branches separated by the FSR D_1. The dashed line represents the comb line array. Where the fit lines are not fully accurate due to lack of measured points, they are gray. (b) Measured single soliton spectrum in resonator device with the above dispersion profile. Observed higher-order DW on high-frequency side matched with points on the corresponding dispersion curves. (c) Experimental comb reconstruction measurement of the soliton comb in the frequency range 184–220 THz.

C. Experimental verification

First, we verify the excitation of higher-order dispersive waves in strongly pulse-driven resonators, that feature periodic dispersion as shown in Fig. 6. The resonator device used here, $R1$, has a relatively cubic dispersion profile with coefficients $D_{1,2,3,4}/2\pi = 15.06$ GHz, 14.3 kHz, 6.59 Hz, and -3.84 mHz respectively, with intrinsic loss and coupling $\kappa_{0,\mathrm{ex}}/2\pi = 30$ and 230 kHz, respectively. The high value of κ_{ex} is used in order to maximize the output power of the soliton spectrum, with a given average power of 720 mW entering the chip waveguide. After the soliton spectrum is generated stably, by tuning the EO-comb center frequency across resonance into the bistability region [4], there appear several Kelly-like sidebands, or HDWs, on the short-wavelength side of the spectrum. Remarkably, these higher-order dispersive waves are observed up to fifth order and appear spectrally highly distinct from the DKS. Extrapolating the DKS envelope, we observe that the HDW exhibits more than 25 dB power compared to the smooth single DKS case. Figure 6(a) shows the integrated dispersion profile of this microresonator measured separately [54], overlaid with its fourth-order polynomial fitting $D_{\mathrm{int}} = \sum_{k=2}^{4} D_k \mu^k/k!$, and five additional orders of D_{int} separated negatively by nD_1. In Fig. 6(b), the final soliton spectrum is plotted featuring HDWs up to the fifth order.

Next, we compare the location of the observed HDWs with the theoretical predictions. By taking the frequencies of each HDW in Fig. 6(b) and projecting them onto each Floquet order of *folded* integrated dispersion operators in Fig. 6(a) (black circles), we retrieve a linear frequency comb grid (black dashed line). This tilted line gives us the soliton comb relative frequency grid whose repetition rate (comb line spacing) is controlled by the injected EO-comb pulse train, desynchronized from the cavity FSR slightly by $f_{\mathrm{eo}} = D_1/2\pi + \delta f_{\mathrm{eo}}$ [15]. We directly confirm the comb integrity using the Kerr comb reconstruction technique [55], which allows us to experimentally obtain a direct measurement of the NDR (see Appendix C for measurement details). The resulting image is shown in Fig. 4(c), measured across the bandwidth available to us of 184–240 THz, although only the first-order dispersive wave has a sufficient signal-to-noise ratio to be captured. The image shows that every comb line of this spectrum lies on a straight grid spaced by 15.059 07 GHz, as sampled in this plot, which does exactly equal the experimentally set EO-comb frequency f_{eo}. In particular, the first HDW seen at 211 THz lies on the very same grid.

It should be pointed out that the soliton spectrum does not match prediction on the long-wavelength side. According to the above dispersion plot, we should see likely two more first-order HDWs, as the comb grid crosses the $D_{L-} - D_1$ operator (approximately $D_{\mathrm{int}} - D_1$; see Appendix B) twice at 169 THz and later below 140 THz. Instead, we see these two features at 148 and 154 THz, indicating the polynomial fitting is inaccurate in this region due to the lack of measured dispersion values beneath 180 THz.

IV. NORMAL DISPERSION CASE

A. Numerical analysis

Next, we discuss the Floquet dynamics of coherent structures in normal dispersion resonators. In this case, the pulsed pumping, used in our experiments to achieve high peak powers, plays another major role in stabilizing SW structures that appear in the resonator. SWs usually have a nonzero relative group velocity that depends on the driving amplitude f^2. However, there is a particular value of f^2 that corresponds to a stationary SW pattern called a Maxwell point [6,56]. Pulse pumping leads to an intracavity power gradient that depends on the intraresonator coordinate φ; therefore, the edges of an SW lock to the part of the pump corresponding to the Maxwell point. The dispersion modulation, in this case, leads to the Faraday instability dynamics including the effect of period doubling [34], resulting in the generation of widely spaced sidebands that originate from the two-dimensional FWM process.

We provide numerical simulations of the LLE Eq. (1) and compare homogeneous and modulated cavity cases. Figures 7(a), 7(b), and 7(d) display the ideal SW generated in a synchronously pumped resonator. Figure 7(a) (yellow) shows a typical platicon profile of a rectangular pulse with oscillating tails. Figure 7(b) is the corresponding spectrum showing the flattop spectral profile. The NDR plotted in Fig. 7(d), particularly the inset, clearly reveals the origin of such a spectrum. Since both branches of the bistable resonance Ψ_L and Ψ_H are involved in the SW formation, we observe all dispersive resonances ζ_{L-}, ζ_{H-}, and ζ_{H+} on the NDR (ζ_{L+} is again too weak to appear). The ζ_{H-} curve originating from the upper state Ψ_H (top of the SW) acquires an additional phase shift due to the Kerr nonlinearity and, therefore, is shifted down to lower frequencies relative to ζ_{L-}. A coherent structure corresponding to the rising and falling edges of the SW acquires a smaller Kerr shift and, therefore, caresses the curve ζ_{L-}. Such a crossing implies phase matching between the states and leads to enhanced power at the crossing modes. This creates the flattened spectral profile of the SW [6,53].

When the SW is generated in the modulated cavity, a strong influence of the FI is observed. Performing numerical simulation with the same parameters as in the soliton section, but with the sign of $d_2^{(0)}$ reversed, we observe *period-doubling* dynamics in Figs. 7(a) and 7(c). The top part of the SW is patterned with periodic structures, similar to that observed in the cw case (Fig. 3), that are direct evidence of FI. Each round-trip, the patterned profile exhibits a π phase flip as reported in Refs. [30,34]. The power profiles $|\Psi(\varphi, t)|^2$ at two stages of the period-doubling dynamics are displayed in Fig. 7(a). The corresponding spectral plot in Fig. 7(b) shows

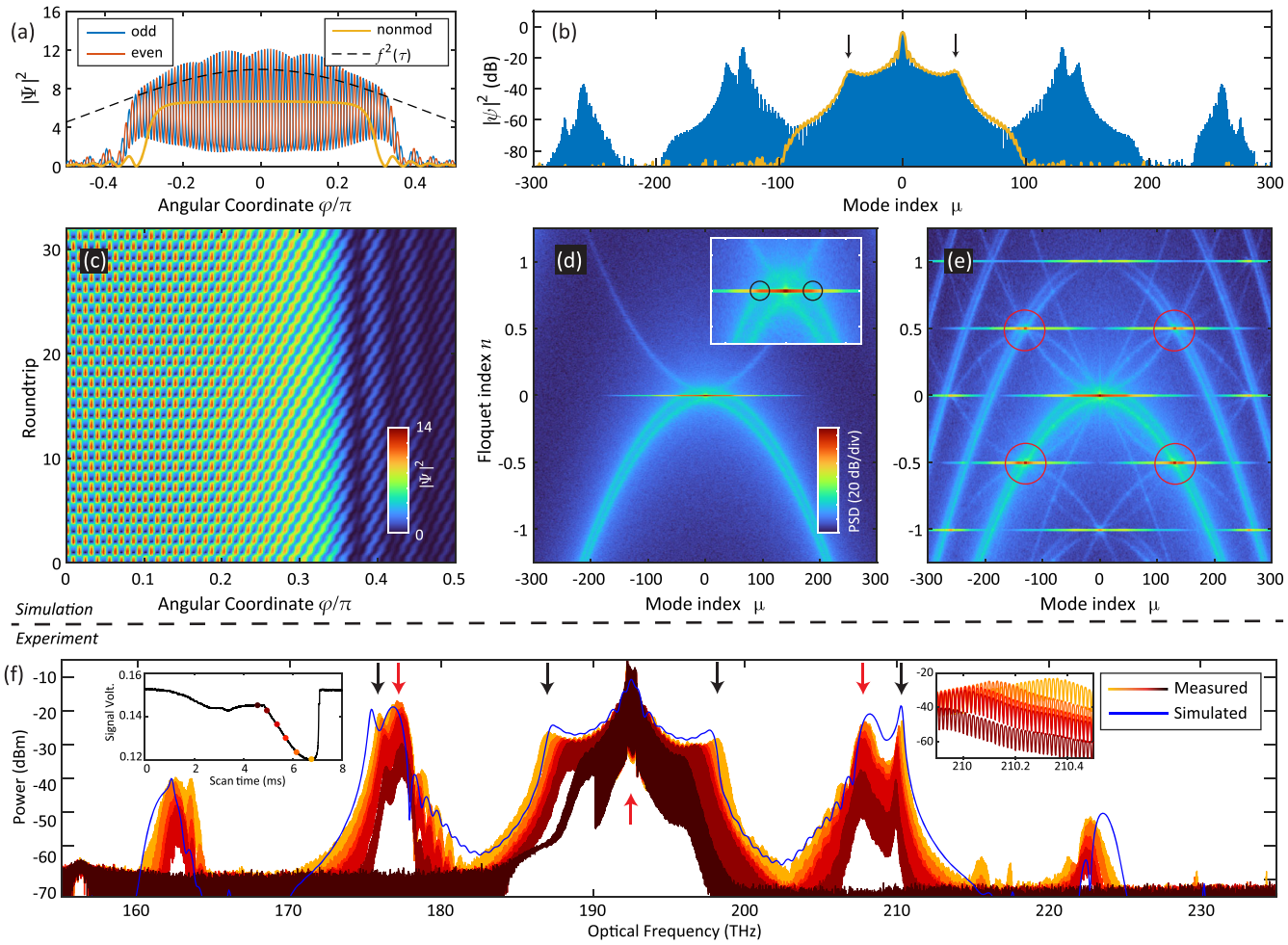

FIG. 7. SW solution in pulse-driven modulated cavity for $f^2 = 10$, $\zeta_0 = 6$, $\Delta = 0.7d_2^{(0)}$, $d_1/2\pi = 16$, and $d_2^{(0)} = 0.0027$. (a) SW field in cavity angular coordinate with (blue) and without (yellow) modulation. (b) Corresponding power spectrum. (c) Spatiotemporal diagram of an SW in the modulated cavity. (d),(e) SW nonlinear dispersion relation, obtained by taking $\mathcal{F}[\,]$ over both dimensions of the spatiotemporal diagram for nonmodulated and modulated cases, respectively. Black circles show the intersections of a SW line and dispersive parabola resulting in the canonical SW spectral profile. Red circles indicate FI-originated satellites. (f) Measured optical spectra of switching wave affected by FI at different detunings (red-orange scale). Simulated spectral envelope overlaid (blue). Left inset: measured cavity power out during scan of laser detuning over resonance. Red and orange points mark locations of measured spectra. Right inset: enlargement of comb lines at outer dispersive wave. Black and red arrows correspond to circles from (d) and (e).

the appearance of characteristic *double-peaked* sideband spectra substantially extending the unperturbed SW spectrum. In a microresonator environment, these sidebands manifest as *satellite combs* drawing energy from the central comb.

Besides the conclusion from the analysis that predicts the position of the modes having maximum FI gain, there is an empirical understanding of the process that can be formulated by analyzing the NDR plot shown in Fig. 7(e). In the normal dispersion case, conventional modulation instability does not affect the upper state of the bistable resonance. Because of the high power, the conjugated upper-state dispersive curve ζ_{H+} becomes visible on the NDR. Both curves are experiencing modulation, resulting in the FSR-spaced Floquet bands. At the location in the n vs μ space where ζ_{H-} and ζ_{H+} cross, we observe the formation of satellites. Because of the apparent mirror symmetry between ζ_{H-} and ζ_{H+}, the intersection occurs at $\pm\mathrm{FSR}/2$ in the slow frequency dimension. As explained above, this process can be seen as a two-dimensional FWM process, providing photon transfer from the pump to the sidebands having an $\pm\mathrm{FSR}/2$ offset. The double-peak structure of subcombs can be readily explained with the NDR. This double feature was, in fact, seen in numerical simulations shown in Staliunas, Hang, and Konotop [31] but was not discussed there in further detail. The coherent subcomb line formed around the unstable mode, sourced from FI, crosses both ζ_{H-} and ζ_{L-} simultaneously, resulting in two peaks, the spacing of which corresponds to the separation between these dispersive curves. A larger 3D

perspective of Fig. 7(e), looking closely at this feature, can be found in Supplemental Material [48].

B. Experimental verification

We present experimental results of a switching wave with satellite comb generation in dispersion-modulated resonators here, with the goal of verifying the coherence and comblike nature of the spectrum as well as the validity of our modeling. For this, two example resonator devices are investigated: $R2$ and $R3$. $R2$ has relatively strong normal and symmetrical dispersion, with $D_{1,2,3,4}/2\pi = 15.32$ GHz, -12.9 kHz, 5.36 Hz, and -2.39 mHz, respectively, and $\kappa_{0,\mathrm{ex}}/2\pi = 30$ and 180 kHz, respectively. $R3$, on the other hand, has a flatter and more imbalanced dispersion profile, with $D_{1,2,3,4}/2\pi = 15.31$ GHz, -3.14 kHz, 3.35 Hz, and -2.49 mHz, respectively, and $\kappa_{0,\mathrm{ex}}/2\pi = 30$ and 200 kHz, respectively. All other experimental details including the driving and detection setup are the same as discussed above in Fig. 5. Further measurements of the resonator parameters can be found in Supplemental Material [48].

In Fig. 7(f), we present satellite comb generation results in $R2$, with an average pump power of 230 mW. The left inset in this figure shows the detected power trace from the output of the cavity, while the laser center frequency is scanned across the cavity resonance from blue detuned to red detuned, showing different stages in the way the trace dips in power. The first dip and plateau correspond to the initial buildup of power in the resonator and the subsequent formation of the switching wave comb by wave breaking [6,53]. The second dip, past halfway, marks the sudden growth of satellite combs. The reason the output power trace decreases in energy during this phase is due to the fact that the photodiode in use does not detect light above 1700 nm (below 176 THz). This indicates energy transfer from the central comb to the satellite comb. As marked with red-to-orange dots, we stop the laser tuning at the several points here and plot the spectra measured. Two large satellite combs are observed to rise quickly, *above* even the plateau comb power of the core switching wave. Each satellite comb consists of two features. On the inner side closer to the core spectrum are the sinc() profilelike spectra, marked with red arrows, that represent the origin of the FI pattern sourced from the "inside" of the switching wave, on its upper state, as shown previously in Fig. 7. These are equispaced about the core spectrum at ± 15.5 THz, due to

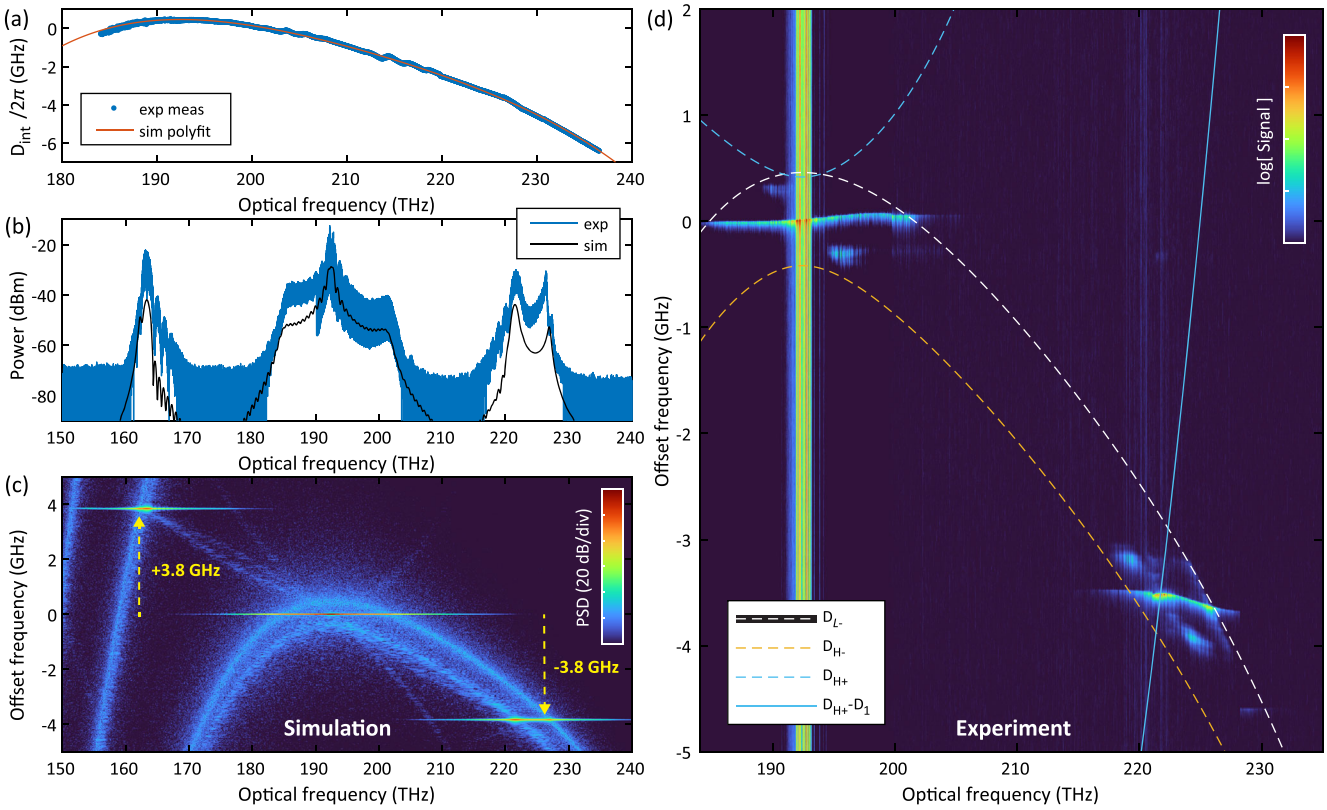

FIG. 8. Phase matching for broadband satellite combs. (a) Experimentally measured integrated dispersion for resonator $R3$, with fourth-order polynomial fit, used in the following simulation. (b) Experimentally measured spectrum of a switching wave with satellite combs, overlaid with simulation result, offset by -15 dB. (c) Nonlinear dispersion relation of the simulation above, showing upper and lower dispersion curves and their higher orders. (d) Experimentally measured comb reconstruction, the equivalent of the image in (c), showing the central comb and short-wavelength satellite located near the predicted phase-matched frequency offset. Overlaid are the analytical dispersion curves used from the simulation. The strong band across 192 THz is excess amplified spontaneous emission from the pump spectrum.

the FI requirement, and appear to agree approximately with the prediction of Eq. (6). The second feature is the sharp hooklike dispersive wave on the outer side of the satellite combs, marked with black arrows. These mark the relative location of the lower-state dispersive resonance D_{L-} (where $D_{L-} = \kappa\zeta_{L-}/2$ in dimensionless) with which the FI spectra interact, as also described above in Fig. 7. Using the independently measured loss and dispersion values of $R2$ given above, we simulate the very same experiment using the LLE with real resonator units. The final simulated spectrum when tuning into resonance is plotted in the same Fig. 7(f) in blue, showing good agreement, particularly with respect to the satellite combs' "double feature." Further results from this simulation can be found in Supplemental Material [48].

Moving on to further explore the phase matching of these satellite combs more deeply, we present measurements and corresponding simulations of generated satellite combs in resonator device $R3$, shown in Fig. 8. The experimental dispersion measurement is shown in Fig. 8(a), and its fitting is used to obtain the dispersion parameters listed above and carry out verification simulations. When tuning the laser to the point of strongest comb generation, we measure the spectrum shown in Fig. 8(b), with average power coupled to the resonator of 60 mW, this time showing satellite comb generation further apart in comparison to Fig. 7(f). Recreating the same experiment in simulation creates the black spectral envelope, showing good agreement. In Fig. 8(c), the NDR image for the simulation state is shown, revealing the coherence of the satellite combs and their precise relative position in offset frequency relative to the central switching wave comb, including the three nonlinear dispersion curves D_{L-}, D_{H-}, and D_{H+} that determine this phase matching. According to this figure, the requirement for the FI gain to be equidistant with the pump, and located on the upper-state dispersion curve, causes the satellite combs to originate at 163 and 222 or ± 29.5 THz relative to the pump, with an offset frequency of ± 3.8 GHz, respectively. In a

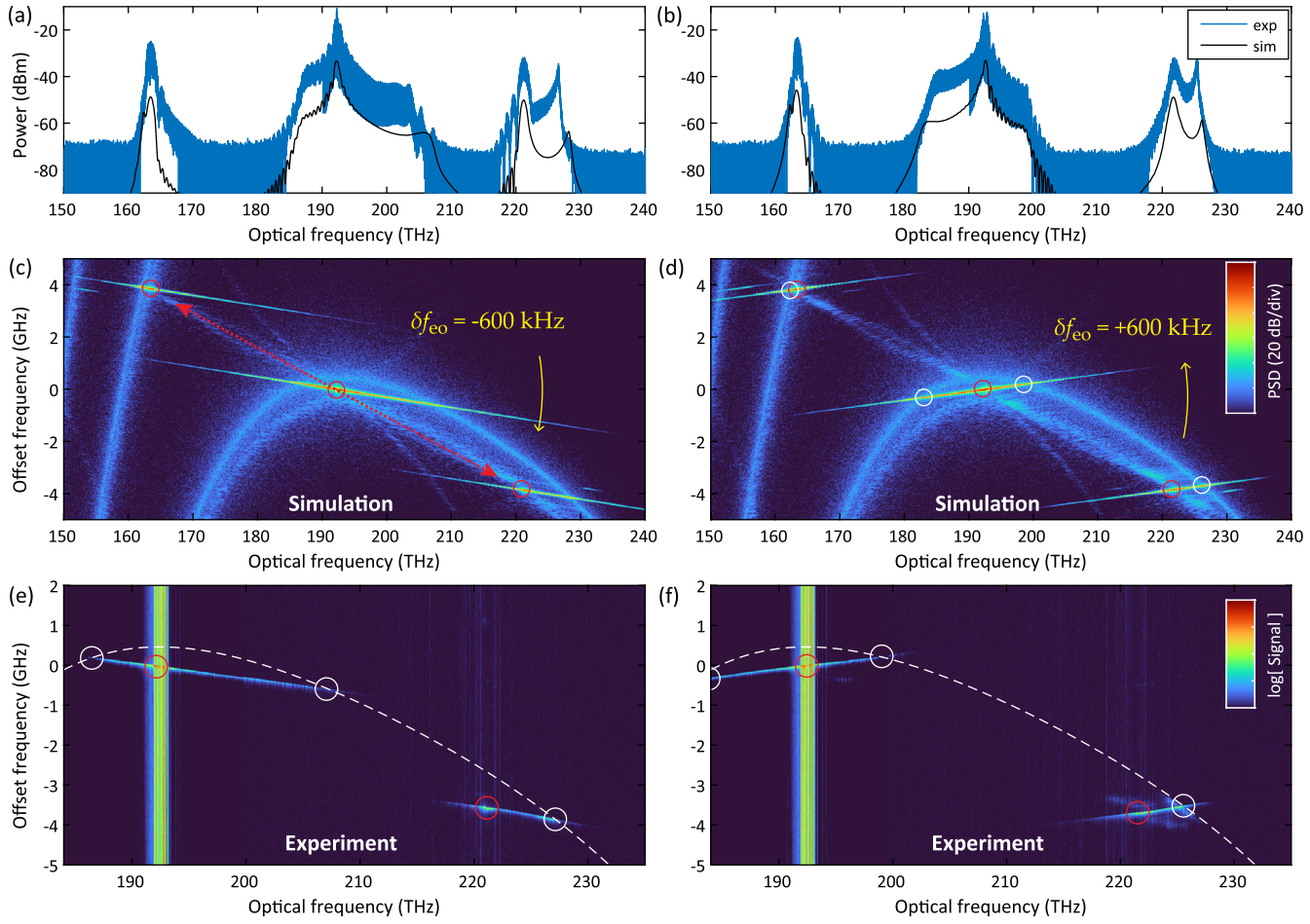

FIG. 9. Satellite comb repetition rate tuning and phase matching. Two switching wave + satellite comb generation events where (a),(c),(e) $\delta f_{eo} = +600$ kHz and (b),(d),(f) $\delta f_{eo} = -600$ kHz. (a),(b) Spectrum, measured, and simulated using measured resonator parameters. Simulated is offset by -15 dB. (c),(d) Nonlinear dispersion relation image for the simulated case showing offset satellite comb spectra. (e),(f) Measured comb reconstruction image. The strong band across 192 THz is excess amplified spontaneous emission from the pump spectrum. The lower nonlinear dispersion curve shown as a dashed white line. Faraday instability gain frequency is marked in red. Dispersive waves are marked in white.

perfectly symmetrical dispersion profile such as in Fig. 7 or close to the experiment for $R2$ in Fig. 7(f), this offset value would be at or near the FSR/2, 7.66 GHz. In $R3$, due to the positive D_3, the dispersion landscape is pulled upward in the positive optical frequency direction, resulting in this frequency offset value of 3.8 GHz.

To confirm our understanding, we perform comb reconstruction (described in Appendix C) and plot the image in Fig. 8(d). The data shown here correspond to the same spectral measurement plotted in Fig. 8(b). Plotted on top are the nonlinear dispersion curves calculated for the simulated parameters: the upper- and lower-state curves D_{H-} and D_{L-}, respectively (dashed), as well as the conjugated upper-state curve D_{H+} (dashed) and its FSR-shifted Floquet band (solid). In real units, $D_{\pm} = \kappa\zeta_{\pm}/2$. In this image, we can see the central SW comb spanning 185–203 THz, and we verify that its spectral wings are bound by the lower-state dispersion curve D_{L-}. Crucially, we verify that the short-wavelength satellite comb appears at an offset frequency of −3.5 GHz, almost where it is predicted to appear according to the simulated model at the intersection of $D_{H-} = D_{H+} - D_1$. The outer dispersive wave wing of the satellite also appears as this comb's intersection with the lower-state dispersion curve D_{L-}. Both combs appear to be coherent, with optical linewidths limited by the detection resolution of the probing laser (approximately 4 MHz). We must acknowledge that the detected offset frequency of each comb line seems to drift up and down by several megahertz across the whole measurement, particularly at the end of the satellite comb. This drift is likely due to slow thermal shifts in the pumped resonator mode spectrum (which is not locked) occurring during the 40-s swept-laser scan. This varies from take to take. It is not indicative of the physical frequency comb.

To complete our demonstration of the nature of the satellite comb offset frequency and its relationship to the dispersion curves, the same series of graphs is presented in Fig. 9. This time, however, the frequency of the EO comb f_{eo}, i.e., the imposed repetition rate of SW generation inside the cavity, is changed between two limits. In the above Fig. 8 results, δf_{eo} is set to 0 in simulation, and in experiment it is set to the point of maximum spectrum symmetry in the wings of the SW comb, with $f_{\mathrm{eo}} = 15.308\,77$ GHz. In Figs. 9(a), 9(c), and 9(e), we downturn f_{eo} by $\delta f_{\mathrm{eo}} = -600$ kHz and in Figs. 9(b), 9(d), and 9(f) upturn by $\delta f_{\mathrm{eo}} = +600$ kHz. In each case, experimentally and in simulation, it is important to observe that the center of FI gain stays *fixed* at ±29.5 THz in the optical axis and at ±3.8 or ±3.5 GHz offset frequency in simulation and experiment, respectively. These points are highlighted by red lines and circles. While these points remain fixed, the repetition rate (comb line spacing) of all combs exactly follows the imposed repetition rate $f_{\mathrm{rep}} = f_{\mathrm{eo}} + \delta f_{\mathrm{eo}}$, causing the visual "tilt" in the combs shown in Figs. 9(c)–9(f). Where the tilted comb spectra cross D_{L-} is where the dispersive waves form, highlighted in white circles. By cross comparing the NDR graphs with the optical spectra shown above in Figs. 9(a) and 9(b), one can see the direct origin of each comb feature.

V. CONCLUSION

In this work, we presented a comprehensive investigation of dissipative structure existence in dispersion-folded Kerr cavities with a fundamental spatial modulation of the dispersion. The source of additional spectral features is shown directly through 2D analysis of four-wave mixing pathways, in simulation via the slow vs fast frequency NDR diagrams and in experiment by the comb reconstruction measurement. For the dissipative soliton, we see directly the appearance of resonant radiation that we term as higher-order dispersive waves, i.e., dispersive waves appearing quasiphase matched to dispersive resonance curves (or Floquet bands) in FSR-folded space. This is termed as such in relation to conventional "zeroth-order" dispersive waves that phase match directly to the base level unmodulated dispersive resonance curve, such as dual-dispersive waves in resonators with quartic dispersion [57].

For the switching wave structure, we showed direct generation of powerful satellite combs born of the Faraday instability from the switching wave upper state, a microcomb structure that to our knowledge has never before been observed. These satellite combs are shown to be mutually locked in repetition rate with the core SW structure. However, the center frequency of each satellite comb is not determined by this repetition rate and is, instead, set fixed by the cavity dispersion, forming at a point up to an FSR/2 offset from the core comb. We showed how the repetition rate is controllable by varying the injected pulse repetition rate. Some of the cited works here instead predicted or observed Faraday instability arising as a result of the modulation of other parameters of the LLE, such as the nonlinear constant [31], and the loss or coupling value [30,58] (via the *Ikeda map* model as opposed to the LLE). All such processes can be analyzed using a similar method. In this work, we have found dispersion modulation to be the sufficient and dominant contributor to the observed phenomena, with a brief analysis of this to be found in Supplemental Material [48].

In terms of applicable value, if assuming that engineering highly flat dispersion is difficult in a given waveguide platform, deliberate modulation of the dispersion instead will automatically generate many higher-order dispersive waves that extend a soliton microcomb spectrum significantly wider beyond the point where the body of the comb disappears into the optical noise floor. Doing so deliberately may extend an already broad soliton microcomb further to the point where it can become octave spanning and able to be f-$2f$ self-referenced [13]. Similarly, and more dramatically, assuming a fixed dispersion profile, dispersion modulation is shown here to effortlessly enable a

switching wave microcomb to be extended by multiple times its base-level bandwidth. Such combs could in the future find use in spectroscopy [59], telecommunications [60], astrospectrometer calibration [12], and LIDAR [10]. For these reasons, longitudinal parametric modulation of the resonator waveguide may become a resource for spectrally extending Kerr microcombs.

The data and code that support the plots and numerical simulations within this paper are available at [61]. Any other data and findings of this study are available from the corresponding author upon reasonable request

ACKNOWLEDGMENTS

This work was supported by Contract No. D18AC00032 (DRINQS) from the Defense Advanced Research Projects Agency (DARPA). This material is based upon work supported by the Air Force Office of Scientific Research under Grant No. FA9550-19-1-0250. This work was further supported by the European Union's Horizon 2020 Program for Research and Innovation under Grant No. 812818 (Marie Skłodowska-Curie ETN MICROCOMB) and by the Swiss National Science Foundation under Grant Agreement No. 192293. We also thank Zheru Qiu for assistance in sample fabrication. All samples were fabricated in the Center of MicroNanoTechnology (CMi) at EPFL.

APPENDIX A: ANALYTICAL APPROACH TO THE MODULATED CAVITY DYNAMICS

1. Nonlinear dispersion operators

The Kerr bistable solutions are found from the roots of the cubic equation of the LLE, at equilibrium where $\partial_t \Psi = 0$, in the absence of any dispersion term:

$$(|\Psi|^2)^3 - 2\zeta_0(|\Psi|^2)^2 + (\zeta_0^2+1)|\Psi|^2 - f^2 = 0 \tag{A1}$$

and, subsequently,

$$\Psi_{\mathrm{cw}} = \frac{if}{|\Psi_{\mathrm{cw}}|^2 - \zeta_0 + i}. \tag{A2}$$

The resulting nonlinear dispersion operators are found from Ref. [43] as follows:

$$\zeta_{L\pm}(\mu) = -\delta d_1\mu + d_3\mu^3 \mp \sqrt{(\zeta_0 - d_2\mu^2 - d_4\mu^4 - 2|\Psi_L|^2)^2 - |\Psi_L|^4}, \tag{A3}$$

$$\zeta_{H\pm}(\mu) = -\delta d_1\mu + d_3\mu^3 \mp \sqrt{(\zeta_0 - d_2\mu^2 - d_4\mu^4 - 2|\Psi_H|^2)^2 - |\Psi_H|^4}, \tag{A4}$$

including orders of dispersion and group velocity shift from d_1 to d_4.

2. Modulation instability analysis

In case of harmonic modulation of the dispersion, Eq. (4) indicates linear coupling between the amplitudes $\tilde{\psi}_{n\mu}$ and $\tilde{\psi}_{n\pm1\mu}$, resulting in breathing of generated structures with period equal to the round-trip time. However, the presence of Kerr nonlinearity gives rise to period multiplication effects that occur due to Faraday instability. In this section, we perform a modulation instability analysis for the period-doubled continuous-wave solution.

We assume $\psi_0(\varphi, t)$ to be a solution of Eq. (1) with an unmodulated dispersion term. We are interested in dynamics of a small perturbation $\xi(\varphi, t)$ that obeys the linearized equation

$$\frac{\partial\xi}{\partial t} = -(1+i\zeta_0)\xi + i\left(d_2^{(0)} + \Delta\frac{e^{id_1t}+e^{-id_1t}}{2}\right)\frac{\partial^2}{\partial\varphi^2}\xi + i(2|\psi_0|^2\xi + \psi_0^2\xi^*) + \Delta\frac{\partial^2\psi_0}{\partial\varphi^2}\cos d_1 t. \tag{A5}$$

First, we use the following ansatz: $\xi = A(t)\exp i\mu\varphi + B^*(t)\exp -i\mu\varphi$, so the coupled equations for the amplitudes A and B read

$$\frac{\partial A}{\partial t} = -(1+i\zeta_0)A - i\left(d_2^{(0)} + \Delta\frac{e^{id_1t}+e^{-id_1t}}{2}\right)\mu^2 A + i(2|\psi_0|^2A + \psi_0^2B) + \Delta\frac{\partial^2\psi_0}{\partial\varphi^2}\cos d_1 t,$$

$$\frac{\partial B}{\partial t} = -(1-i\zeta_0)B + i\left(d_2^{(0)} + \Delta\frac{e^{id_1t}+e^{-id_1t}}{2}\right)\mu^2 B - i(2|\psi_0|^2B + \psi_0^2A) + \Delta\frac{\partial^2\psi_0}{\partial\varphi^2}\cos d_1 t.$$

We continue, assuming $A = \alpha_+\exp id_1t/2 + \alpha_-\exp -id_1t/2$ and $B = \beta_+\exp id_1t/2 + \beta_-\exp -id_1t/2$, where the amplitudes obey

$$\frac{d}{dt}\mathbb{Y} = \mathbb{M}\mathbb{Y}, \tag{A6}$$

where $\mathbb{Y} = [\alpha_+, \alpha_-, \beta_+, \beta_-]^T$ and the matrix

$$\mathbb{M} = \begin{pmatrix} y_{00} & -i\mu^2\Delta/2 & i\psi_0^2 & 0 \\ -i\mu^2\Delta/2 & y_{11} & 0 & i\psi_0^2 \\ -i\psi_0^{*2} & 0 & y_{00}^* & i\mu^2\Delta/2 \\ 0 & -i\psi_0^{*2} & i\mu^2\Delta/2 & y_{11}^* \end{pmatrix}, \tag{A7}$$

where $y_{00} = -(1+i\zeta_0) - id_1/2 - i\mu^2 d_2^{(0)} + 2i|\psi_0|^2$ and $y_{11} = y_{00} + id_1$. The real part of the eigenvalues of this

matrix give the parametric gain of modulationally unstable solutions. Comb indices of these solutions can be approximated by the following formula:

$$\mu = \pm \sqrt{\frac{d_1}{2\sqrt{(d_2^{(0)})^2 - (\Delta/2)^2}}}. \tag{A8}$$

APPENDIX B: NUMERICAL MODELING

To model the dynamics of the field envelope in periodically varying dispersion resonators, we numerically solve Eq. (1) in normalized units using the well-known split-step method [40]. This is for the studies presented in Figs. 2–4 and 7. For Figs. 7(f), 8, and 9, the real experimental results are replicated in simulations using the system model with practical units:

$$\frac{\partial A}{\partial t'} = \mathcal{F}_\tau[i(\delta\omega + 2\pi\mu\delta f_{\mathrm{eo}} + D_{\mathrm{int}}(t',\mu))\tilde{A}_\mu] - \frac{\kappa}{2}A + i\Gamma|A|^2A + f_p(\tau)\sqrt{\frac{D_1\kappa_{\mathrm{ex}}}{2\pi}P_0} \tag{B1}$$

acting on field (in $\sqrt{W}$) $A(t',\tau)$ over slow or laboratory time t' and fast time τ in the comoving frame of the intracavity field circulating at D_1, with frequency domain counterpart $\tilde{A}_\mu$ at discrete comb line indices μ. The linear phase operators include the detuning $\delta\omega$, the desynchronization of the pulse drive with the cavity field δf_{eo}, and the dispersion operator that varies with time as

$$D_{\mathrm{int}}(t',\mu) = (1 + \Delta\cos(D_1 t'))\left[\frac{D_2}{2}\mu^2 + \frac{D_3}{6}\mu^3 + \frac{D_4}{24}\mu^4\right]. \tag{B2}$$

The loss and coupling rates satisfy $\kappa = \kappa_0 + \kappa_{\mathrm{ex}}$, and the nonlinear coupling parameter $\Gamma = D_1 n_2 \omega_0 L/(2\pi c A_{\mathrm{eff}})$ for resonator length L, effective waveguide area A_{eff}, and nonlinear refractive index n_2. The injected pulse profile has a peak power P_0. All parameters here are found experimentally and can be related to the dimensionless values by the following transformations: $t = t'\kappa$, $\varphi = \tau D_1$, $\Psi = A\sqrt{2\Gamma/\kappa}$, $d_l = 2D_l/(\kappa l!)$ for $l = 1$–4, $\zeta_0 = 2\delta\omega/\kappa$, and $f^2 = 4P_0\kappa_{\mathrm{ex}}\Gamma D_1/(\pi\kappa^3)$. The experimental nonlinear dispersion curves are related to the dimensionless curves by $\zeta_\pm(\mu) = 2D_\pm(\mu)/\kappa$. All parameter values used to reconstruct the field dynamics are presented in Supplemental Material [48].

APPENDIX C: EXPERIMENTAL DETAIL

1. Chip pumping

The experimental setup for characterization of nonlinear frequency mixing and dissipative Kerr soliton generation combines the experimental setups used in Ref. [55] for Kerr comb reconstruction and Ref. [22] for dissipative soliton generation and EO-comb control. A widely tunable external cavity diode laser is passed through three fiber-coupled phase modulators and one amplitude modulator, all synchronously driven by an rf synthesizer (Rhode & Schwarz SMB100A) set to near the FSR. The 1.4-ps pulses are formed after traveling through approximately 275 m of SMF-28, then amplified in an erbium-doped fiber amplifier, and coupled to the photonic chip through lens fibers with 2.4-dB insertion loss.

2. Comb reconstruction

This technique is realized on the linear dispersion measurement tool [54] reconfigured to a heterodyne optical spectrum analyzer by superimposing the output of the resonator with the scanning laser on a balanced photodetector. Kerr comb reconstruction provides a high spectral resolution (of the order of 4 MHz) and an extended dynamic range (enhanced by a multistage logarithmic amplifier—Analog Devices 8307), which allow us to obtain full spectral information about the generated comb state. The diagram of this measurement method is shown in Supplemental Material [48].

[1] G. Nicolis and I. Prigogine, *Self-Organization in Nonequilibrium Systems, From Dissipative Structures to Order through Fluctuations* (Wiley, New York, 1977), p. 339.

[2] T. J. Kippenberg, A. L. Gaeta, M. Lipson, and M. L. Gorodetsky, *Dissipative Kerr Solitons in Optical Microresonators*, Science **361**, eaan8083 (2018).

[3] L. Chang, S. Liu, and J. E. Bowers, *Integrated Optical Frequency Comb Technologies*, Nat. Photonics **16**, 95 (2022).

[4] T. Herr, V. Brasch, J. D. Jost, C. Y. Wang, N. M. Kondratiev, M. L. Gorodetsky, and T. J. Kippenberg, *Temporal Solitons in Optical Microresonators*, Nat. Photonics **8**, 145 (2014).

[5] X. Xue, Y. Xuan, Y. Liu, P. H. Wang, S. Chen, J. Wang, D. E. Leaird, M. Qi, and A. M. Weiner, *Mode-Locked Dark Pulse Kerr Combs in Normal-Dispersion Microresonators*, Nat. Photonics **9**, 594 (2015).

[6] M. H. Anderson, W. Weng, G. Lihachev, A. Tikan, J. Liu, and T. J. Kippenberg, *Zero Dispersion Kerr Solitons in Optical Microresonators*, Nat. Commun. **13**, 4764 (2022).

[7] X. Xue, Y. Xuan, P.-H. Wang, Y. Liu, D. E. Leaird, M. Qi, and A. M. Weiner, *Normal-Dispersion Microcombs Enabled by Controllable Mode Interactions*, Laser Photonics Rev. **9**, L23 (2015).

[8] J. Feldmann, N. Youngblood, M. Karpov, H. Gehring, X. Li, M. Stappers, M. Le Gallo, X. Fu, A. Lukashchuk, A. S. Raja, J. Liu, C. D. Wright, A. Sebastian, T. J. Kippenberg, W. H. Pernice, and H. Bhaskaran, *Parallel Convolutional Processing Using an Integrated Photonic Tensor Core*, Nature (London) **589**, 52 (2021).

[9] P. Trocha, M. Karpov, D. Ganin, M. H. Pfeiffer, A. Kordts, S. Wolf, J. Krockenberger, P. Marin-Palomo, C. Weimann,

S. Randel, W. Freude, T. J. Kippenberg, and C. Koos, *Ultrafast Optical Ranging Using Microresonator Soliton Frequency Combs*, Science **359**, 887 (2018).

[10] J. Riemensberger, A. Lukashchuk, M. Karpov, W. Weng, E. Lucas, J. Liu, and T. J. Kippenberg, *Massively Parallel Coherent Laser Ranging Using a Soliton Microcomb*, Nature (London) **581**, 164 (2020).

[11] P. Marin-Palomo, J. N. Kemal, M. Karpov, A. Kordts, J. Pfeifle, M. H. Pfeiffer, P. Trocha, S. Wolf, V. Brasch, M. H. Anderson, R. Rosenberger, K. Vijayan, W. Freude, T. J. Kippenberg, and C. Koos, *Microresonator-Based Solitons for Massively Parallel Coherent Optical Communications*, Nature (London) **546**, 274 (2017).

[12] E. Obrzud, M. Rainer, A. Harutyunyan, M. H. Anderson, J. Liu, M. Geiselmann, B. Chazelas, S. Kundermann, S. Lecomte, M. Cecconi, A. Ghedina, E. Molinari, F. Pepe, F. Wildi, F. Bouchy, T. J. Kippenberg, and T. Herr, *A Microphotonic Astrocomb*, Nat. Photonics **13**, 31 (2019).

[13] D. T. Spencer, T. Drake, T. C. Briles, J. Stone, L. C. Sinclair, C. Fredrick, Q. Li, D. Westly, B. R. Ilic, A. Bluestone, N. Volet, T. Komljenovic, L. Chang, S. H. Lee, D. Y. Oh, M.-G. Suh, K. Y. Yang, M. H. P. Pfeiffer, T. J. Kippenberg, E. Norberg, L. Theogarajan, K. Vahala, N. R. Newbury, K. Srinivasan, J. E. Bowers, S. A. Diddams, and S. B. Papp, *An Optical-Frequency Synthesizer Using Integrated Photonics*, Nature (London) **557**, 81 (2018).

[14] Z. L. Newman, V. Maurice, T. Drake, J. R. Stone, T. C. Briles, D. T. Spencer, C. Fredrick, Q. Li, D. Westly, B. R. Ilic, B. Shen, M.-G. Suh, K. Y. Yang, C. Johnson, D. M. S. Johnson, L. Hollberg, K. J. Vahala, K. Srinivasan, S. A. Diddams, J. Kitching, S. B. Papp, and M. T. Hummon, *Architecture for the Photonic Integration of an Optical Atomic Clock*, Optica **6**, 680 (2019).

[15] E. Obrzud, S. Lecomte, and T. Herr, *Temporal Solitons in Microresonators Driven by Optical Pulses*, Nat. Photonics **11**, 600 (2017).

[16] A. S. Raja, A. S. Voloshin, H. Guo, S. E. Agafonova, J. Liu, A. S. Gorodnitskiy, M. Karpov, N. G. Pavlov, E. Lucas, R. R. Galiev, A. E. Shitikov, J. D. Jost, M. L. Gorodetsky, and T. J. Kippenberg, *Electrically Pumped Photonic Integrated Soliton Microcomb*, Nat. Commun. **10**, 1 (2019).

[17] B. Stern, X. Ji, Y. Okawachi, A. L. Gaeta, and M. Lipson, *Battery-Operated Integrated Frequency Comb Generator*, Nature (London) **562**, 401 (2018).

[18] G. Moille, E. F. Perez, J. R. Stone, A. Rao, X. Lu, T. S. Rahman, Y. K. Chembo, and K. Srinivasan, *Ultra-Broadband Kerr Microcomb through Soliton Spectral Translation*, Nat. Commun. **12**, 7275 (2021).

[19] S.-P. Yu, D. C. Cole, H. Jung, G. T. Moille, K. Srinivasan, and S. B. Papp, *Spontaneous Pulse Formation in Edgeless Photonic Crystal Resonators*, Nat. Photonics **15**, 461 (2021).

[20] A. Tikan, J. Riemensberger, K. Komagata, S. Hönl, M. Churaev, C. Skehan, H. Guo, R. N. Wang, J. Liu, P. Seidler, and T. J. Kippenberg, *Emergent Nonlinear Phenomena in a Driven Dissipative Photonic Dimer*, Nat. Phys. **17**, 604 (2021).

[21] O. B. Helgason, F. R. Arteaga-Sierra, Z. Ye, K. Twayana, P. A. Andrekson, M. Karlsson, J. Schröder, and Victor Torres-Company, *Dissipative Solitons in Photonic Molecules*, Nat. Photonics **15**, 305 (2021).

[22] M. H. Anderson, R. Bouchand, J. Liu, W. Weng, E. Obrzud, T. Herr, and T. J. Kippenberg, *Photonic Chip-Based Resonant Supercontinuum via Pulse-Driven Kerr Microresonator Solitons*, Optica **8**, 771 (2021).

[23] K. Luo, Y. Xu, M. Erkintalo, and S. G. Murdoch, *Resonant Radiation in Synchronously Pumped Passive Kerr Cavities*, Opt. Lett. **40**, 427 (2015).

[24] A. U. Nielsen, B. Garbin, S. Coen, S. G. Murdoch, and M. Erkintalo, *Invited Article: Emission of Intense Resonant Radiation by Dispersion-Managed Kerr Cavity Solitons*, APL Photonics **3**, 120804 (2018).

[25] S. Kelly, *Characteristic Sideband Instability of Periodically Amplified Average Soliton*, Electron. Lett., **28**, 806 (1992).

[26] J. Peng and H. Zeng, *Build-Up of Dissipative Optical Soliton Molecules via Diverse Soliton Interactions*, Laser Photonics Rev. **12**, 1800009 (2018).

[27] W. Zhao, C. Yang, and M. Shen, *Enhanced Kelly Sidebands of Mode-Locking Fiber Lasers for Efficient Terahertz Signal Generation*, Opt. Laser Technol. **137**, 106802 (2021).

[28] C. Wang, B. Chang, T. Tan, C. Qin, Z. Wu, G. Yan, B. Fu, Y. Wu, Y. Rao, H. Xia, and B. Yao, *High Energy and Low Noise Soliton Fiber Laser Comb Based on Nonlinear Merging of Kelly Sidebands*, Opt. Express **30**, 23556 (2022).

[29] T. B. Benjamin and F. Ursell, *The Stability of the Plane Free Surface of a Liquid in Vertical Periodic Motion*, Proc. R. Soc. A **225**, 505 (1954).

[30] S. Coen and M. Haelterman, *Modulational Instability Induced by Cavity Boundary Conditions in a Normally Dispersive Optical Fiber*, Phys. Rev. Lett. **79**, 4139 (1997).

[31] K. Staliunas, C. Hang, and V. V. Konotop, *Parametric Patterns in Optical Fiber Ring Nonlinear Resonators*, Phys. Rev. A **88**, 023846 (2013).

[32] M. Conforti, A. Mussot, A. Kudlinski, and S. Trillo, *Modulational Instability in Dispersion Oscillating Fiber Ring Cavities*, Opt. Lett. **39**, 4200 (2014).

[33] A. Mussot, M. Conforti, S. Trillo, F. Copie, and A. Kudlinski, *Modulation Instability in Dispersion Oscillating Fibers*, Adv. Opt. Photonics **10**, 1 (2018).

[34] F. Bessin, F. Copie, M. Conforti, A. Kudlinski, A. Mussot, and S. Trillo, *Real-Time Characterization of Period-Doubling Dynamics in Uniform and Dispersion Oscillating Fiber Ring Cavities*, Phys. Rev. X **9**, 041030 (2019).

[35] F. Copie, M. Conforti, A. Kudlinski, A. Mussot, and S. Trillo, *Competing Turing and Faraday Instabilities in Longitudinally Modulated Passive Resonators*, Phys. Rev. Lett. **116**, 143901 (2016).

[36] J. Yang, S.-W. Huang, Z. Xie, M. Yu, D.-L. Kwong, and C. W. Wong, *Coherent Satellites in Multispectral Regenerative Frequency Microcombs*, Commun. Phys. **3**, 1 (2020).

[37] C.-X. Zhu, W. Yi, G.-C. Guo, and Z.-W. Zhou, *Parametric Resonance of a Bose-Einstein Condensate in a Ring Trap with Periodically Driven Interactions*, Phys. Rev. A **99**, 023619 (2019).

[38] M. J. Ablowitz and J. T. Cole, *Transverse Instability of Rogue Waves*, Phys. Rev. Lett. **127**, 104101 (2021).

[39] V. Zakharov and A. Rubenchik, *Instability of Waveguides and Solitons in Nonlinear Media*, Zh. Eksp. Teor. Fiz. **65**, 997 (1973), https://www.math.arizona.edu/~zakharov/papers/pdf/ZakharovRubenchikJETP1973.pdf.

[40] G. P. Agrawal, in *Nonlinear Fiber Optics*, sixth ed., edited by G. P. Agrawal (Academic, New York, 2019), Chap. 2, pp. 27–55.

[41] K. P. Leisman, D. Zhou, J. W. Banks, G. Kovačič, and D. Cai, *Effective Dispersion in the Focusing Nonlinear Schrödinger Equation*, Phys. Rev. E **100**, 022215 (2019).

[42] A. Tikan, F. Bonnefoy, G. Ducrozet, G. Prabhudesai, G. Michel, A. Cazaubiel, É. Falcon, F. Copie, S. Randoux, and P. Suret, *Nonlinear Dispersion Relation in Integrable Turbulence*, Sci. Rep. **12**, 10386 (2022).

[43] C. Milián and D. V. Skryabin, *Soliton Families and Resonant Radiation in a Micro-Ring Resonator near Zero Group-Velocity Dispersion*, Opt. Express **22**, 3732 (2014).

[44] Y. He, S. Wang, and X. Zeng, *Dynamics of Dispersive Wave Emission from Dark Solitons in Kerr Frequency Combs*, IEEE Photonics J. **8**, 1 (2016).

[45] Y. K. Chembo and C. R. Menyuk, *Spatiotemporal Lugiato-Lefever Formalism for Kerr-Comb Generation in Whispering-Gallery-Mode Resonators*, Phys. Rev. A **87**, 053852 (2013).

[46] M. Haelterman, S. Trillo, and S. Wabnitz, *Dissipative Modulation Instability in a Nonlinear Dispersive Ring Cavity*, Opt. Commun. **91**, 401 (1992).

[47] S.-W. Huang, A. K. Vinod, J. Yang, M. Yu, D.-L. Kwong, and C. W. Wong, *Quasi-Phase-Matched Multispectral Kerr Frequency Comb*, Opt. Lett. **42**, 2110 (2017).

[48] See Supplemental Material at http://link.aps.org/supplemental/10.1103/PhysRevX.13.011040 for additional descriptions of the measurement method and extended numerical simulations on dissipative structure formation.

[49] J. Liu, G. Huang, R. N. Wang, J. He, A. S. Raja, T. Liu, N. J. Engelsen, and T. J. Kippenberg, *High-Yield, Wafer-Scale Fabrication of Ultralow-Loss, Dispersion-Engineered Silicon Nitride Photonic Circuits*, Nat. Commun. **12**, 1 (2021).

[50] A. Kordts, M. H. P. Pfeiffer, H. Guo, V. Brasch, and T. J. Kippenberg, *Higher Order Mode Suppression in High-Q Anomalous Dispersion* SiN *Microresonators for Temporal Dissipative Kerr Soliton Formation*, Opt. Lett. **41**, 452 (2016).

[51] S.-W. Huang, H. Liu, J. Yang, M. Yu, D.-L. Kwong, and C. W. Wong, *Smooth and Flat Phase-Locked Kerr Frequency Comb Generation by Higher Order Mode Suppression*, Sci. Rep. **6**, 26255 (2016).

[52] M. Fujiwara, M. Teshima, J. Kani, H. Suzuki, N. Takachio, and K. Iwatsuki, *Optical Carrier Supply Module Using Flattened Optical Multicarrier Generation Based on Sinusoidal Amplitude and Phase Hybrid Modulation*, J. Lightwave Technol. **21**, 2705 (2003).

[53] Y. Xu, Y. Xu, A. Sharples, A. Sharples, J. Fatome, J. Fatome, J. Fatome, S. Coen, S. Coen, M. Erkintalo, M. Erkintalo, S. G. Murdoch, and S. G. Murdoch, *Frequency Comb Generation in a Pulse-Pumped Normal Dispersion Kerr Mini-resonator*, Opt. Lett. **46**, 512 (2021).

[54] J. Liu, V. Brasch, M. H. P. Pfeiffer, A. Kordts, A. N. Kamel, H. Guo, M. Geiselmann, and T. J. Kippenberg, *Frequency-Comb-Assisted Broadband Precision Spectroscopy with Cascaded Diode Lasers*, Opt. Lett. **41**, 3134 (2016).

[55] T. Herr, K. Hartinger, J. Riemensberger, C. Wang, E. Gavartin, R. Holzwarth, M. Gorodetsky, and T. Kippenberg, *Universal Formation Dynamics and Noise of Kerr-Frequency Combs in Microresonators*, Nat. Photonics **6**, 480 (2012).

[56] P. Parra-Rivas, D. Gomila, E. Knobloch, S. Coen, and L. Gelens, *Origin and Stability of Dark Pulse Kerr Combs in Normal Dispersion Resonators*, Opt. Lett. **41**, 2402 (2016).

[57] M. H. P. Pfeiffer, C. Herkommer, J. Liu, H. Guo, M. Karpov, E. Lucas, M. Zervas, and T. J. Kippenberg, *Octave-Spanning Dissipative Kerr Soliton Frequency Combs in* Si_3N_4 *Microresonators*, Optica **4**, 684 (2017).

[58] M. Conforti, F. Copie, A. Mussot, A. Kudlinski, and S. Trillo, *Parametric Instabilities in Modulated Fiber Ring Cavities*, Opt. Lett. **41**, 5027 (2016).

[59] N. Picqué and T. W. Hänsch, *Frequency Comb Spectroscopy*, Nat. Photonics **13**, 146 (2019).

[60] A. Fülöp, M. Mazur, A. Lorences-Riesgo, Ó. B. Helgason, P.-H. Wang, Y. Xuan, D. E. Leaird, M. Qi, P. A. Andrekson, A. M. Weiner, and V. Torres-Company, *High-Order Coherent Communications Using Mode-Locked Dark-Pulse Kerr Combs from Microresonators*, Nat. Commun. **9**, 1598 (2018).

[61] M. Anderson, A. Tikan, A. Tusnin, J. Riemensberger, A. Davydova, R. N. Wang, and T. J. Kippenberg, *Dissipative Solitons and Switching Waves in Dispersion-Modulated Kerr Cavities*, Zenodo (2023), 10.5281/zenodo.7696283.